ChemistrySelect

Research Article
doi.org/10.1002/slct.202502160

Chemistry Europe
European Chemical Societies Publishing

www.chemistryselect.org

Enhancing Hydrogen Evolution in Water Splitting with Pectin Stabilized Magnetite Nanoparticles

Nompumelelo N. Shibe,[a] Zandile Mhlwatika,[a] Shankara G Radhakrishnan,[a] and Nolwazi Nombona*[a]

Magnetite (Fe_3O_4) nanoparticles are used in heterogeneous catalysis due to their biocompatibility, magnetic properties, and catalytic activity. However, Fe_3O_4 is prone to oxidation, which can compromise its structural and chemical stability. To address this, pectin, a biodegradable biopolymer extracted from agricultural waste, was used as a stabilizing agent to enhance the structural integrity of Fe_3O_4 nanoparticles. The nanoparticles were synthesized using a co-precipitation method and characterized using FTIR, XRD, SEM, and BET, and further evaluated as catalysts for electrochemical water splitting. FTIR confirmed the interaction between carboxyl groups in pectin and Fe_3O_4, indicating successful incorporation of pectin into the nanoparticles. Pectin-coated (Fe_3O_4@Pect) and uncoated Fe_3O_4 nanoparticle sizes were determined to be 11.55 and 5.20 nm, respectively, with surface areas of 52 and 71 m^2/g. Electrocatalytic performance toward the hydrogen evolution reaction (HER) was assessed using linear sweep voltammetry (LSV) under near-acidic and alkaline environments. The catalytic activity showed dependence on pH, which influenced current densities and stability. The findings suggest that the performance of Fe_3O_4@Pect is governed by pectin stability and surface transformations under alkaline conditions, which improved performance. This work presents pectin as a sustainable material to improve the stability and catalytic efficiency of Fe_3O_4 nanoparticles for HER.

1. Introduction

Securing clean energy while combusting remains a global challenge.[1] Currently, fossil fuels including oil and coal, dominate energy systems, but their combustion releases billions of tons of greenhouse gases, accelerating climate change and global warming.[2] These nonrenewable sources are being rapidly depleted by rising energy demands, necessitating a transition to sustainable alternatives.[3] The transition to renewable energy offers a way to delay the depletion of fossil fuels.[4] Hydrogen (H_2) has emerged as a promising clean and sustainable energy solution owing to its high gravimetric energy density, renewability, and zero carbon emissions upon use.[5–7] Conventional hydrogen production remains largely dependent on fossil fuel reforming, but renewable methods are increasingly being explored to meet sustainability goals. Among these, photoelectrochemical (PEC) water splitting has attracted considerable attention as a viable long-term solution.[8,9] Recent advances in PEC catalyst design, such as the incorporation of dual-metal-atom sites like Fe–Ir pairs on hematite, have demonstrated exceptional potential by enhancing interfacial charge transfer, accelerating reaction kinetics, and reducing recombination losses. These improvements have significantly advanced solar-to-hydrogen conversion efficiency.[10] Such innovations are critical for making green hydrogen economically viable at scale.

Water splitting is considered environmentally friendly as it uses renewable energy sources.[8] It establishes a sustainable cycle by electrochemically splitting water into hydrogen and oxygen through hydrogen evolution and oxygen evolution (OER) reactions.[9] However, these processes are limited by sluggish reaction kinetics due to high overpotentials, sensitivity to pH, poor catalyst efficiency, and reliance on scarce and expensive platinum group metals.[11] This challenge has driven ongoing research into the development of sustainable and cost-effective electrocatalysts to improve overall energy efficiency.[12,13] For example, recent studies have demonstrated that photoelectrochemical systems extend beyond conventional water splitting by enabling the simultaneous production of value-added chemicals such as disinfectants directly from seawater, while maintaining sustainable operating conditions.[13]

Earth-abundant transition metal-based catalysts have gained considerable interest as sustainable alternatives, particularly iron oxide nanoparticles, which have been successfully used as heterogeneous catalysts due to their biocompatibility, cost-effectiveness, and electrical conductivity.[14,15] Research into Fe_3O_4, especially its α-phase (hematite), has grown extensively over the last two decades, primarily driven by its potential in sustainable energy applications, especially in PEC water splitting.[16] Hematite's abundance, chemical stability, nontoxicity, and narrow band gap (~2.1 eV) make it a promising photoanode material for splitting water into hydrogen and oxygen using solar energy.[17,18] Its capacity to absorb visible light up to 600 nm

[a] N. N. Shibe, Z. Mhlwatika, S. G Radhakrishnan, N. Nombona
Department of Chemistry, University of Pretoria, Private Bag X20, Hatfield, Pretoria 0028, South Africa
E-mail: nolwazi.nombona@up.ac.za

Supporting information for this article is available on the WWW under https://doi.org/10.1002/slct.202502160 and its favorable alignment of the valence band with the oxygen evolution potential have made it a central focus in solar fuel research.[19,20]

Despite its advantages, Fe_3O_4 faces significant intrinsic limitations that impair its photoelectrochemical performance. Its poor electrical conductivity and short hole diffusion length (~2–4 nm) lead to rapid charge carrier recombination, especially near the surface, reducing the photo-conversion efficiency.[21,22] Additionally, hematite suffers from relatively slow OER kinetics due to sluggish charge transfer across the semiconductor–electrolyte interface.[23] To address these issues, strategies such as doping, nanostructuring, heterojunction formation, and co-catalyst deposition have been employed. Doping with elements such as Ti or Co helps improve conductivity and modulate the electronic band structure.[24] In one study, atomic-level platinum (Pt) doping significantly improved hematite photoanodes by enhancing carrier lifetime, suppressing recombination, and increasing OER efficiency.[25] Further evidence of enhancement is seen in Cr-N co-doped Fe_3O_4 catalysts which exhibited lower overpotentials (95 mV at 10 mA cm^{-2}) compared to undoped Fe_3O_4 (280.1 mV), highlighting superior catalytic activity and stability.[26] Highly conductive Fe_3O_4@graphite composites have also shown excellent HER performance with an overpotential of 120 mV and a Tafel slope of 78 mV dec^{-1}, indicating improved kinetics and stability.[27] Similar improvements can be achieved through structural modifications such as nanostructuring, which increases surface area and shortens charge transport paths.[28,29] For instance, a composite of SnO_2 nanostructures anchored onto α-Fe_2O_3, significantly enhanced charge separation, improved conductivity, and boosted photocurrent density by facilitating better interfacial contact and reduced diffusion paths.[30] Interface engineering through heterojunctions or surface modifications has also been shown to enhance interfacial charge separation.[31] This was clearly demonstrated in a study where a heterojunction between α-Fe_2O_3 and NiFe layered double hydroxide (LDH) significantly enhanced PEC performance. The resulting heterostructure facilitated interfacial charge separation and minimized recombination, resulting in a higher photocurrent and a lower onset potential.[32] Recent advances have demonstrated the efficacy of MOF-derived bimetallic composites, such as iron-modified ZIF-67-based electrocatalysts, in improving OER performance.[33] Moreover, ZIF@$CoFe_2O_4$ composites demonstrated superior activity for water splitting (105 mV at 10 mA cm^{-2}, Tafel slope 43 mV dec^{-1}). These findings highlight the exciting prospect of high-performance, noble metal-free electrocatalysts for low-cost, efficient, and sustainable hydrogen production.[34]

Despite these promising modifications, Fe_3O_4 still faces critical challenges as a HER catalyst, including instability under different pH conditions and insufficient high-density active sites for effective hydrogen adsorption.[35,36] These limitations, combined with the complexity and cost of many enhancement techniques, hinder their scalability and sustainability. As a result, green chemistry and biopolymer-based approaches have emerged as attractive alternatives. Polysaccharides such as pectin, which is derived from plant cell walls, are biocompatible, biodegradable, and water-soluble. Their –OH and –COOH groups enable them to bind metal ions and guide nanoparticle formation.[37] When used to coat or stabilize Fe_3O_4, they enhance surface dispersion, modulate electronic properties, and form protective matrices that resist photo-corrosion and dissolution.[38,39] Bio-assisted syntheses are typically performed in aqueous media at low temperatures, avoiding toxic reagents and energy-intensive steps.[40] Integrating pectin with Fe_3O_4 offers a sustainable and scalable strategy to overcome intrinsic barriers. The biopolymer layer acts as a molecular interface modifier, tuning surface electronic properties and improving interaction with the electrolyte. Furthermore, pectin enables green synthesis routes that align with broader goals of eco-friendly energy technology.

While Fe_3O_4@Pect nanoparticles have already shown utility in diverse fields like water purification,[41] drug delivery systems,[42] and general electrochemical catalysis,[43–45] their specific capabilities as HER and OER electrocatalysts are still unexplored. This work, therefore, seeks to address this gap by evaluating Fe_3O_4@Pect composites for electrochemical water splitting, with the aim of advancing sustainable green hydrogen production.

2. Materials and Methods

2.1. Materials

All chemicals were used as received from the suppliers. Pectin was extracted from orange peels. Ethanol (EtOH) was purchased from Enterprise. Iron (II) sulfate heptahydrate ($FeSO_4.7H_2O$), iron (III) chloride hexahydrate ($FeCl_3.6H_2O$), ammonium hydroxide (NH_4OH), potassium sulfate (K_2SO_4), and potassium hydroxide (KOH) were bought from Sigma-Aldrich. Nafion D-521 (5 wt %) was purchased from Alfa Aesar. Sodium hydroxide (NaOH), sodium chloride (NaCl), and hydrochloric acid (HCl) were purchased from Merck. Distilled water was used throughout this work.

2.2. Instrumentation

The ultrasonic cell disruptor, USCG-2000 (Bioevopeak Co. Ltd.), was used for pectin extraction. A muffle furnace (KJ-MC1100-12Z, Zhengzhou) operated at 600 °C was used to determine the ash content of the extracted pectin. Fourier transform infrared (FTIR) spectra were obtained using a Bruker FTIR-8300 spectrophotometer with a single reflectance ATR platinum diamond accessory within the 4000–400 cm^{-1} range with a resolution of 4 cm^{-1}. The crystallographic structure of the samples was identified by powder X-ray diffraction (PXRD) using a Bruker D2 Phaser using Cu K_α radiation (λ = 1.5406 Å). The patterns were collected within the diffraction angle $2\theta = 10°$ to 90°. Zeiss 540 Ultra plus field emission gun scanning electron microscope (FEG-SEM) operated at 100 nm, 1.2 kV was used to analyze the morphology of the samples. A Quorum Q150 S/E/E/S coater was used to coat samples onto aluminum stubs prior to SEM analysis. Energy-dispersive X-ray (EDX) spectra were obtained from a 540 Zeiss Ultra Plus scanning electron microscope equipped with a field emission gun. A Quantachrome Autosorb iQ was employed to measure the BET surface area of the samples using the multipoint BET method within the relative pressure (P/P0) range from 0.05 to 0.3 P/P0. The pore size distribution was determined using the Barret–Joyner–Halender (BJH) method. A Metrohm PGSTAT (Autolab, AUT72839) controlled by NOVA 2.1 electrochemistry software was used for electrochemical studies.

2.3. Pectin Extraction and Synthesis of Fe_3O_4 Nanoparticles

Pectin was extracted using a previously reported method with slight modifications.[46] Briefly, orange peel powder was immersed in acidified distilled water at pH 1.5. The mixture was sonicated for 10 min at 60 °C and filtered to obtain crude pectin. The crude pectin was precipitated at 25 °C using 98% EtOH. The precipitate was filtered, washed with EtOH and dried in an oven at 30 °C. The dry pectin sample was ground and stored for characterization. Pectin yield was calculated according to Equation (1).

$$\text{Yield} = \frac{m_i}{m_f} \times 100\% \tag{1}$$

where m_i is the mass of peel powder in grams (g) and m_f is the mass (g) of dry pectin powder.

2.3.1. Synthesis of Uncoated Fe_3O_4

A co-precipitation method previously reported was used to synthesize uncoated Fe_3O_4 nanoparticles.[47] A 100 mL solution containing $FeSO_4.7H_2O$ (0.10 M) and $FeCl_3.6H_2O$ (0.20 M) was prepared using previously degassed distilled water. NH_4OH solution was added to the mixture under constant stirring until a black precipitate formed at pH 10. The precipitate was heated at 80 °C for 30 min, washed with distilled water, and dried in an oven at 70 °C.

2.3.2. Synthesis of Fe_3O_4@Pect

Fe_3O_4@Pect was synthesized following a reported procedure.[48] In short, a pectin solution was prepared by dissolving 5.0 mM of pectin in 50 mL of distilled water under constant stirring while bubbling with N_2 gas. Separately, an iron precursor solution was prepared by dissolving $FeSO_4.7H_2O$ (0.29 M) and $FeCl_3.6H_2O$ (0.58 M) in a 1:2 molar ratio in degassed distilled water, followed by stirring for 10 min under an inert atmosphere. The iron solution was added dropwise to the pectin solution while stirring under an inert atmosphere. Thereafter, NH_4OH was added dropwise to the mixture until a black precipitate formed, while maintaining the pH at 10 under an inert atmosphere. The precipitate was collected and washed several times with distilled water until the pH dropped to 7. The product was then dried in an oven at 70 °C, milled into a fine powder, and stored.

2.4. Characterization of the Extracted Pectin

The degree of esterification (DE), the anhydrouronic acid content (AUA), and ash content were used to determine the chemical characteristics of the extracted pectin.[49] DE was calculated using Equation (2), and AUA was calculated using Equation (3).

$$\text{DE}\ (\%) = \frac{V_2}{V_1 + V_2} \times 100 \tag{2}$$

where V_1 is the titrant volume from the first titration and V_2 is the titrant volume from the second titration.

$$\text{AUA}\ (\%) = \frac{176 \times 0.1\,(y+z) \times 100}{W_{(\text{pectin})} \times 1000} \tag{3}$$

where y is the volume of the second titer in mL and z is the volume of the first titer in mL. $W_{(\text{pectin})}$ is the mass of dry pectin in grams.

The ash content was calculated using Equation (4), following the standard procedure.[50]

$$\text{Ash content} = \frac{m_{\text{ash}}\ (\text{g})}{m_{\text{dry pectin initial}}\ (\text{g})} \tag{4}$$

where m_{ash} is the amount of ash after calcination in grams and $m_{\text{dry pectin initial}}$ is the amount of pectin calcined.

2.5. Electrocatalytic Measurements

The catalytic activity of uncoated Fe_3O_4 and Fe_3O_4@Pect was evaluated using electrochemical techniques to assess their potential as electrocatalysts for the hydrogen evolution reaction. Cyclic voltammetry (CV) was employed to investigate the redox behavior of the catalysts. Electrochemical measurements were performed using a conventional three-electrode system comprising a glassy carbon electrode (GCE) as the working electrode, a platinum wire as the counter electrode, and an Ag/AgCl (1.0 M KCl) electrode as the reference. CV measurements were conducted in the potential range of −1.9 V to + 1.9 V at a scan rate of 5.0 mV·s^{-1}.

Electrochemical impedance spectroscopy (EIS) was performed at −0.48 V versus RHE over a frequency range from 0.01 Hz to 10 kHz with an AC amplitude of 5.0 mV in 0.1 M KOH electrolyte. LSV was conducted in the potential window of 0.0 V to −1.80 V at a scan rate of 5.0 mV·s^{-1}. All potentials were converted to the reversible hydrogen electrode (RHE) scale using Equation (5):

$$V_{\text{RHE}} = V_{\text{Ag/AgCl}} + (0.059 \times \text{pH}) + 0.235\,\text{V} \tag{5}$$

where V_{RHE} refers to the potential in the RHE scale, 0.235 V is the potential of the Ag/AgCl electrode versus SHE at 25 °C, and $V_{\text{Ag/AgCl}}$ is the measured potential value in the experiment against the Ag/AgCl reference electrode.[51]

Catalyst inks were prepared by mixing 5 mg of each catalyst with 0.05 mL of 5 wt % Nafion and 0.95 mL of EtOH. The mixtures were stirred for one hour and sonicated for another hour to ensure a uniform suspension. The prepared catalyst ink was drop-cast onto a GCE and allowed to air-dry at room temperature. The 0.1 M K_2SO_4 and 0.1 M KOH solutions were prepared as the electrolytes.

Tafel slopes were determined by fitting the linear regions of the Tafel plots according to Equation (6)

$$\eta = b \log j + a \quad (6)$$

where η is the overpotential in mV, *a* is the exchange current density (mA/cm^2), *j* is the current density in mA/cm^2, and b is the Tafel slope in mV/dec.[52]

3. Results and Discussion

3.1. Physicochemical Characteristics of Pectin

Ultrasonic treatment was used to extract pectin from orange peels. The extracted pectin was used as a coating agent for Fe_3O_4 nanoparticles. The extracted pectin achieved a 31.71% yield, which is comparable to the 32.52% reported in the literature.[53]

To ensure an effective catalyst coating, pectin characteristics such as DE, AUA, and ash content were evaluated. The DE influences gelation behavior and solubility, and it determines the structural and conformational variations of pectin.[54–56] Pectin with DE $>$ 50% is classified as high DE pectin, whereas DE $<$ 50% indicates low DE pectin.[57] As DE decreases, the flexibility of the pectin molecular chain reduces, leading to greater rigidity, whereas a higher DE results in greater molecular flexibility and increased hydrating volume.[58] The pectin extracted in this study had a DE of 66.25%, classifying it as a high DE pectin. This implies a greater ability to form ionic interactions with Fe_3O_4, thereby improving nanoparticle stability.[56] The extracted pectin contained 33.75% of free carboxylate groups that are key for forming strong interactions with Fe_3O_4.

AUA and ash content were used to evaluate the purity of pectin.[59] Pectin extracts with AUA below 65% AUA and ash content above 10% are considered impure.[60] The pectin extracted in this study showed a high AUA content of 87.13% and a low ash content of 0.98% indicating high purity and abundant active functional groups, particularly carboxylate ions.[61,62] The low ash content further confirms purity by reducing inorganic mineral content that could interfere with catalyst performance.[63] Therefore, the extracted pectin can stabilize Fe_3O_4 and enhance its catalytic performance.

3.2. Structural Characteristics of Pectin, Uncoated Fe_3O_4, and Fe_3O_4@Pect

3.2.1. Fourier Transform Infrared Spectroscopy (FTIR)

The FTIR analysis was performed on the extracted pectin, uncoated Fe_3O_4, and Fe_3O_4@Pect nanoparticles to investigate the functional groups of the individual materials (pectin and Fe_3O_4) and their synergistic effect within the Fe_3O_4@Pect composite (Figure 1). The pectin spectrum (Figure 1a) shows a broad peak at 3293 cm^{-1} corresponding to hydroxy (—OH) stretching vibrations attributed to —OH groups on the pyranose ring of the pectin backbone.[64] A peak at 2921 cm^{-1} arises from C—H stretching of CH_2 groups in the galacturonic acid (GalA) units.[65] The vibration band at 1725 cm^{-1} corresponds to carbonyl (—C=O) stretching from the methyl ester (—$COCH_3$) groups, while the vibration band at 1639 cm^{-1} is assigned to the stretching of —COO^- groups.[66] The dominance of the C=O ester stretching peak over the COO^- asymmetric stretching band indicates a high degree of esterification, reflecting a greater proportion of esterified carboxyl groups relative to free carboxylates.[67] A peak at 1010 cm^{-1} is attributed to C—O—C vibrations from glycosidic linkages between pectin monosaccharide units.[68]

In the uncoated Fe_3O_4 spectrum (Figure 1b), bands at 3363 and 1633 cm^{-1} are assigned to —OH stretching and bending vibrations from surface adsorbed water.[69,70] A peak at 1434 cm^{-1} corresponds to N—H bending from residual NH_4OH, while the band at 1096 cm^{-1} is attributed to the asymmetric stretching of SO_4^{2-} from $FeSO_4 \cdot 7H_2O$.[71,72] The Fe—O stretching vibration appears at 541 cm^{-1}.[73] In the Fe_3O_4@Pect spectrum (Figure 1c), characteristic peaks at 1576 and 1396 cm^{-1} correspond to the asymmetric and symmetric stretching of COO^-–Fe bonds, confirming coordination between pectin and the Fe_3O_4 surface.[74,75] A band at 1015 cm^{-1} is associated with C—O—C glycosidic linkages from the pectin backbone,[76] while a sharp peak at 554 cm^{-1} is assigned to Fe–O stretching vibrations.[77] These spectral features collectively indicate successful surface modification of Fe_3O_4 with pectin, as schematically illustrated in Figure 1d, highlighting the functional groups involved in the interaction.

3.2.2. X-ray Diffraction (XRD)

The crystalline phases and diffraction planes of the extracted pectin and synthesized nanoparticles were examined using X-ray diffraction (XRD), with the results presented in Figure 2. The diffractogram of pectin (Figure 2a) exhibited peaks at $2\theta = 12°$, 16°, 21°, and 35°, where the relative sharpness of certain peaks indicates the semi-crystalline nature of pectin, consistent with previous reports.[78] The XRD pattern of uncoated Fe_3O_4 (Figure 2b) displayed distinct diffraction peaks at $2\theta = 30°$, 36°, 43°, 54°, 57°, and 63°, corresponding to the (220), (311), (400), (422), (511), and (440) planes of the spinel magnetite structure.[79] The XRD pattern of Fe_3O_4@Pect, shown in Figure 2c, retained most of the characteristic diffraction peaks of pristine Fe_3O_4, confirming that the magnetite crystal structure was largely preserved following pectin coating.[80] A distinct peak at $2\theta = 12°$ was attributed to the presence of pectin in the composite.[81] Notably, the peak at $2\theta = 55°$, which is clearly observed in uncoated Fe_3O_3, was absent in the Fe_3O_4@Pect sample. This disappearance may result from surface masking by the pectin layer, disruption of surface crystallinity, or diminished diffraction from smaller coherent domains. As previously reported for other biopolymer-coated systems, such structural modifications can attenuate or suppress specific XRD peaks due to decreased crystallinity or reduced long-range order.[82,83] In the composite material, the diffraction peaks appeared slightly broader than those of the uncoated Fe_3O_4, suggesting an increase in amorphous character (Figure 2c). Amorphous materials are known to exhibit enhanced electrocatalytic activity compared to their crystalline counterparts, primarily due to the presence of surface defects

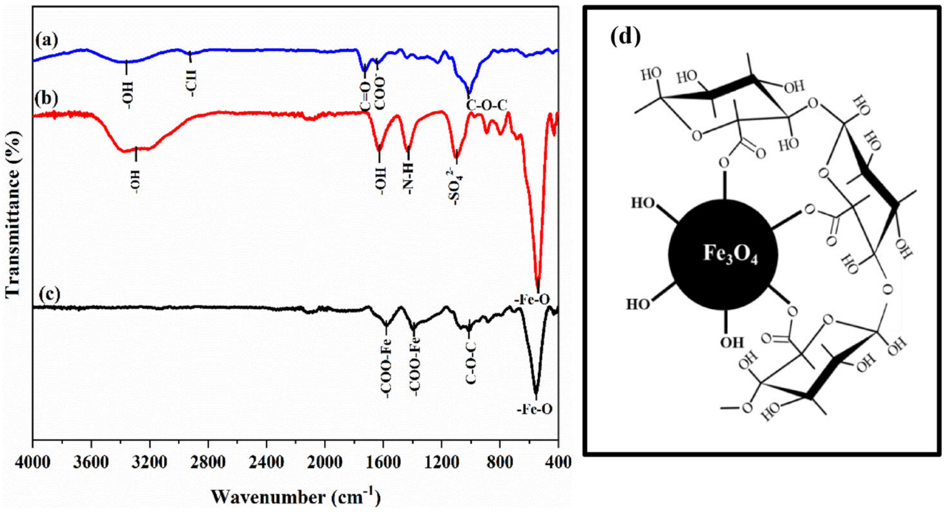

Figure 1. FTIR spectra of a) extracted pectin, b) uncoated Fe_3O_4, c) Fe_3O_4@Pect, and d) an illustration of the interaction between Fe_3O_4 and pectin.

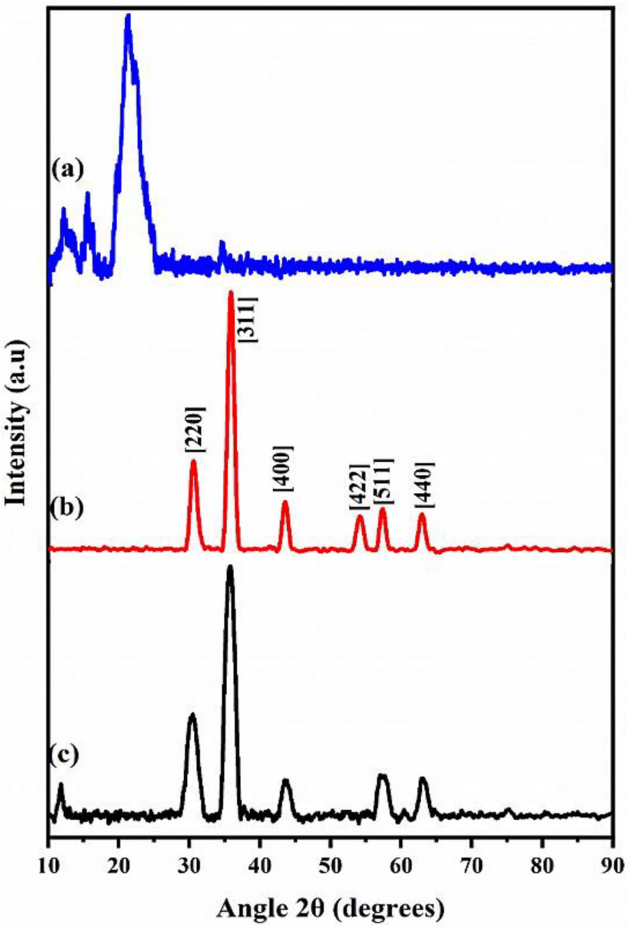

Figure 2. XRD pattern of a) pectin, b) uncoated Fe_3O_4, and c) Fe_3O_4@Pect.

and coordinatively unsaturated sites. However, this increase in catalytic activity may come at the expense of reduced electrical conductivity.[84] To further examine the structural characteristics, the average crystallite size of the composite was calculated using Scherrer's equation (Equation 7)

$$d = \frac{K\lambda}{\beta \cos\theta} \tag{7}$$

where d is the average crystallite size in nanometers (nm), $K = 0.9$ is the Scherrer constant, λ is the x-ray diffraction wavelength ($\lambda = 1.5406$ Å), β is the full width at half maximum (FWHM) of plane (311) and θ is the Bragg angle in degrees.[85] The crystallite size of uncoated Fe_3O_4 was 5.20 nm, whereas Fe_3O_4@Pect exhibited a larger crystallite size of 11.55 nm. This increase suggests the formation of a pectin shell around the Fe_3O_4 nanoparticles, indicating successful surface coating.

3.3. Morphology and Elemental Composition

3.3.1. Scanning Electron Microscopy-Electron Dispersive X-ray Spectroscopy (SEM-EDX)

Morphological analysis provides valuable insight into the permeability, catalytic efficacy, and stability of materials.[86] In this study, SEM-EDX analysis was employed to investigate the surface morphology and elemental compositions of the materials studied. The SEM micrographs revealed distinct surface morphologies for pectin, uncoated Fe_3O_4, and Fe_3O_4@Pect (Figure 3a–c). The pectin sample (Figure 3a) displayed a wrinkled surface, likely resulting from ultrasonic disruption of plant tissue or altered crosslinking between pectic molecules during extraction.[87] Similar surface features have been reported for pectin extracted from citrus albedo and flavedo using microwave-assisted methods, as well as from pomelo peels processed via ultrasonication.[88,89] The uncoated Fe_3O_4 nanoparticles (Figure 3b) exhibited spherical morphology with a high degree of aggregation and relatively uniform shape. In contrast, the Fe_3O_4@Pect nanoparticles (Figure 3c) displayed rougher, more uneven surfaces and a clustered appearance, likely due to the pectin coating. Elemental analysis by EDX (Figure 3d,e) confirmed the presence of Fe and O, verifying the formation of Fe_3O_4 in both uncoated and coated samples. Trace amounts of Cl and S originated from precursor chemicals, while Si signals were attributed to the silicon wafer substrate used for SEM imaging.

Research Article
doi.org/10.1002/slct.202502160

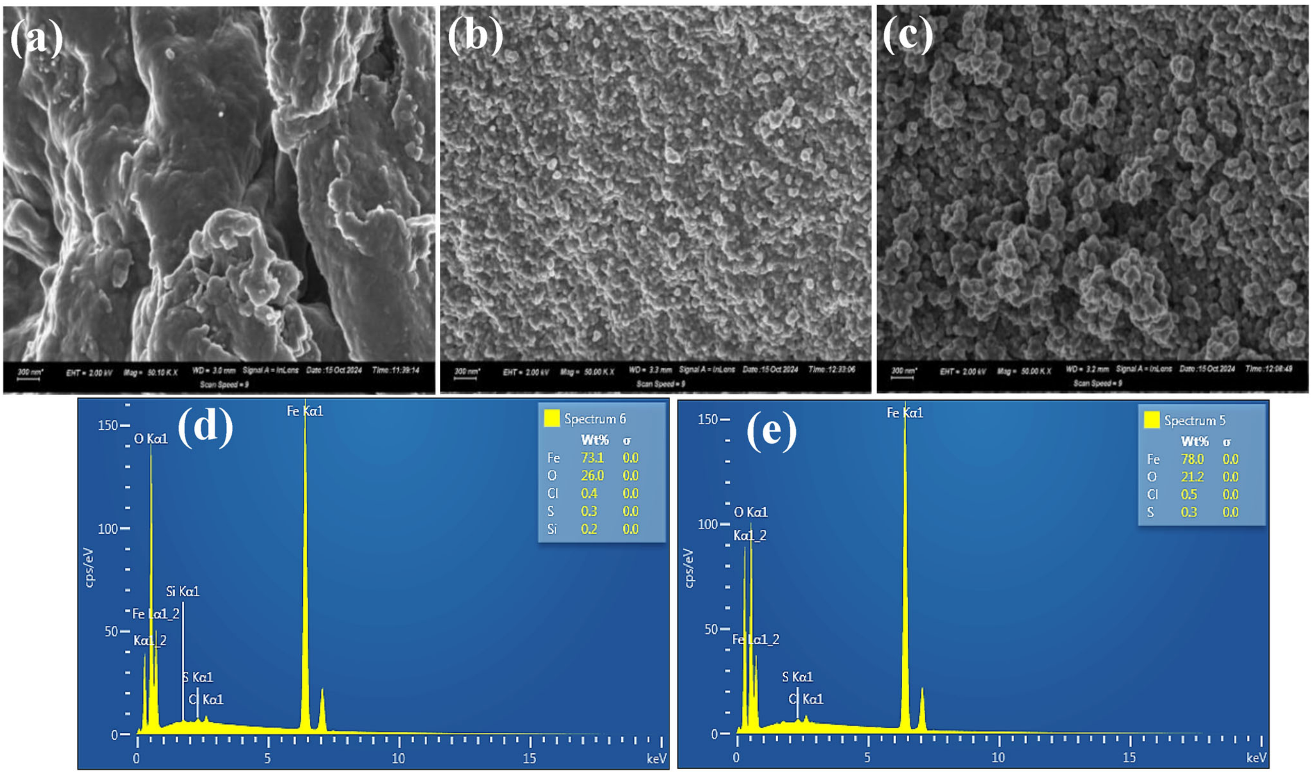

Figure 3. Surface micrographs of a) pectin, b) uncoated Fe_3O_4, c) Fe_3O_4@Pect, and EDX spectrum of d) uncoated Fe_3O_4, and e) Fe_3O_4@Pect.

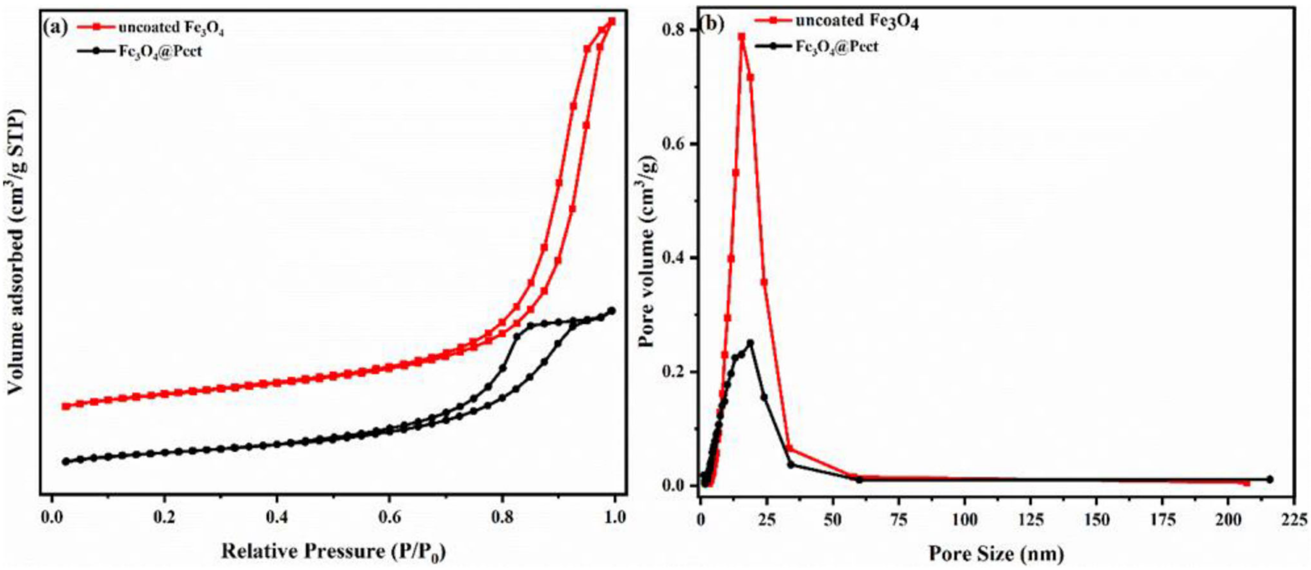

Figure 4. a) N_2 adsorption–desorption isotherms for uncoated Fe_3O_4 (red), and Fe_3O_4@Pect (black) and b) pore size distribution curves for uncoated Fe_3O_4 (red), and Fe_3O_4@Pect (black).

3.4. N_2 Adsorption–Desorption Isotherms

The Brunauer–Emmett–Teller (BET) technique was used to evaluate the surface area, average pore diameter, and pore volume of uncoated Fe_3O_4 and Fe_3O_4@Pect nanoparticles, as shown in Figure 4, with textural properties summarized in Table 1. The nitrogen adsorption–desorption isotherms for both samples exhibited type IV behavior with H3 hysteresis loops (Figure 4a), characteristic of mesoporous materials.[90] The uncoated Fe_3O_4 nanoparticles displayed a BET surface area of 71.09 m^2/g, an average pore diameter of 23.93 nm, and a total pore volume of 0.369 cm^3/g, consistent with previously reported values.[91] As shown in Figure 4b, the pore volume increased with increasing pore diameter, reaching a maximum at 23.93 nm, which is within the mesoporous range.[92] In comparison, the Fe_3O_4@Pect composite exhibited a reduced BET surface area of 52.44 m^2/g, with a

Table 1. Textual properties of the synthesized nanoparticles.		
Characteristic	Uncoated Fe_3O_4	Fe_3O_4@Pect
BET Surface area (m^2/g)	71.09	52.44
Pore diameter (nm)	23.93	10.03
Pore volume (cm^3/g)	0.37	0.16

BJH pore diameter of 10.03 nm and a total pore volume of 0.155 cm^3/g. This reduction in surface area, pore size, and pore volume is attributed to partial pore blockage and surface coverage by pectin molecules, confirming successful surface modification.[93]

3.5. Electrochemical Characterization

Cyclic voltammetry was employed to investigate the electrochemical behavior of the iron oxide nanoparticles, as shown in Figure 5. Both uncoated Fe_3O_4 and Fe_3O_4 @Pect were evaluated in 0.1 M K_2SO_4 (pH 6.37) and 0.1 M KOH (pH 12.83) electrolytes. Figures 5a,c present the full potential windows in K_2SO_4 and KOH, respectively, while Figures 5b,d display the corresponding magnified views of the cathodic region.

In the near-acidic electrolyte (Figure 5a,b), both materials exhibit distinct redox features. The uncoated Fe_3O_4 nanoparticles display one anodic peak and a quasi-reversible cathodic couple centred around ~ -0.2 V versus RHE, which falls within the hydrogen evolution reaction potential range. These peaks are associated with the surface Fe^{2+}/Fe^{3+} redox transitions, arising from reversible oxidation and reduction processes at the nanoparticle–electrolyte interface during ion intercalation and deintercalation.[94,95] The Fe_3O_4 @Pect nanoparticles, however, displayed the cathodic peak at a lower potential ($\sim$0.011 V versus RHE). This shift in potential suggests that the pectin coating is changing the redox behavior of the nanoparticles. This change may reflect enhanced electron transfer kinetics or modified surface interactions, both of which could contribute to improved electrocatalytic activity toward the hydrogen evolution reaction.

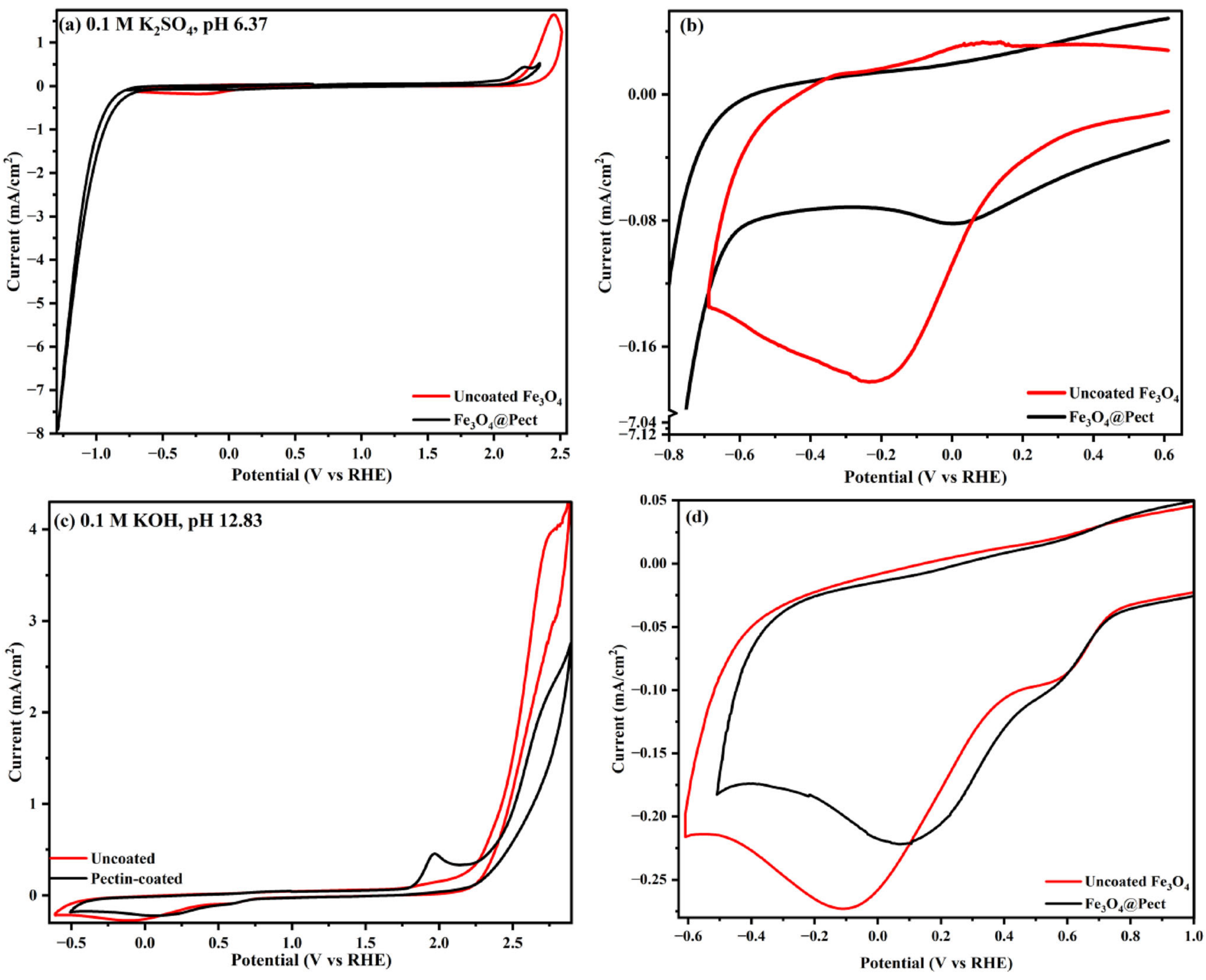

Figure 5. Cyclic voltammograms of uncoated Fe_3O_4 (red) and Fe_3O_4@Pect (black) recorded at a scan rate of 5.0 mV·s^{-1}. a) Full potential window in 0.1 M K_2SO_4 (pH 6.37), b) magnified view of the cathodic region from (a), highlighting redox behavior under near-acidic conditions, c) full potential window in 0.1 M KOH (pH 12.83), and d) magnified view of the cathodic region from (c), highlighting redox behavior under alkaline conditions.

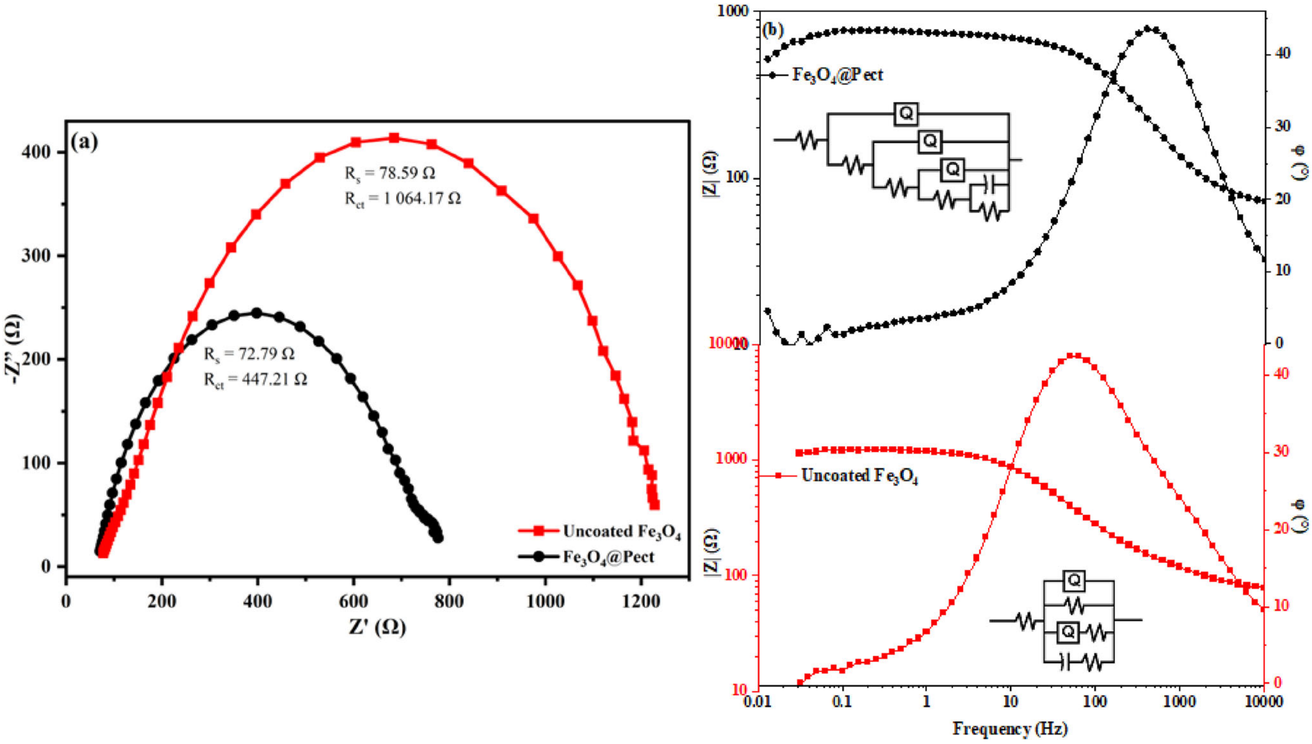

Figure 6. a) Nyquist plots of uncoated Fe_3O_4 (red) and Fe_3O_4@Pect (black) recorded in KOH at open-circuit potential; b) the corresponding Bode plots with the Randle's fitted equivalent circuits.

Furthermore, Fe_3O_4@Pect demonstrates a more capacitive-like CV response compared to the uncoated sample. The smoother, broader current profile and reduced peak sharpness, particularly in the cathodic region, suggest improved charge storage behavior consistent with double-layer capacitance. This capacitive character indicates more efficient ion transport and surface accessibility. The biopolymer coating likely enhances wettability and dispersion, thereby exposing more active sites and facilitating faster charge transfer, making Fe_3O_4@Pect a more effective electrocatalyst than the uncoated nanoparticles.

In the basic environment (0.1 M KOH), shown in Figure 5c,d, both uncoated Fe_3O_4 and Fe_3O_4 @Pect nanoparticles exhibit anodic and cathodic features similar to those observed under near-acidic conditions. Two irreversible cathodic peaks are evident for both samples; however, Fe_3O_4 @Pect displays the more pronounced cathodic peak at a lower potential (~0.1 V versus RHE). This shift in peak potential suggests that the pectin coating enhances electron transfer kinetics or modifies surface interactions under alkaline conditions, both of which likely contribute to improved electrocatalytic activity toward the HER. Also, the uncoated Fe_3O_4 nanoparticles show a more pronounced peak shape, indicating slower kinetics and less efficient electron/ion transport compared to the Fe_3O_4@Pect catalyst.

Electrochemical impedance spectroscopy (EIS) was employed to evaluate the interfacial charge transfer properties of uncoated Fe_3O_4 and Fe_3O_4 @Pect nanoparticles. The resulting Nyquist plots were fitted using equivalent Randles circuit models to extract quantitative electrochemical parameters, as shown in Figure 6a. The shape and features of the Nyquist plots provide insights into the physicochemical processes occurring at the electrode–electrolyte interface, including charge transfer resistance, double-layer capacitance, and ion diffusion dynamics.[96] The EIS measurements were conducted at the onset potential in 0.1 M KOH, applying a potential of −0.48 V versus RHE. Both uncoated Fe_3O_4 and Fe_3O_4@Pect exhibited characteristic semicircular Nyquist plots, indicative of a system dominated primarily by charge transfer resistance (R_{ct}) and double-layer capacitance (C_{dl}). The presence of well-defined semicircles suggests that interfacial electron transfer processes dominate the electrochemical behavior under these conditions. No linear Warburg tail was visible, meaning diffusion does not dominate the impedance in the tested frequency range.

Quantitative analysis was performed by fitting the impedance data to a Randles equivalent circuit model, as illustrated in Figure 6a. The uncoated Fe_3O_4 sample exhibited a large semicircle in the Nyquist plot, indicative of a relatively high charge transfer resistance (R_{ct}) and limited interfacial electron transfer. In contrast, the Fe_3O_4 @Pect electrode displayed a significantly smaller semicircle, reflecting a lower R_{ct} and more efficient charge transfer kinetics.[97] This reduction in resistance can be attributed to the pectin coating, which likely improves electrical conductivity and facilitates faster electron transport at the electrode–electrolyte interface.[98] The pectin coating possibly enhances surface wettability, promotes better dispersion of Fe_3O_4 nanoparticles, and increases the accessibility of electroactive sites at the electrode–electrolyte interface.[98,99] Cyclic voltammetry results showed modest capacitive currents for both materials. Despite this, the reduced R_{ct} observed for Fe_3O_4@Pect suggests an improvement in electrochemically accessible surface area and more efficient charge transport at the interface. A comparable observation was reported by Chen et al.,[100] where hydrophilic functional groups derived from pomelo peel improved surface wettability and electrolyte diffusion, leading to increased electroactive area and reduced R_{ct}.

The electrochemical impedance behavior of uncoated Fe_3O_4 and Fe_3O_4@Pect was further evaluated using Bode plot analysis (Figure 6b). These plots display both the impedance magnitude (|Z|) and phase angle (ϕ) versus frequency, providing insight into the resistive, capacitive, and diffusional contributions of each system.[101] The impedance–magnitude plots (|Z| versus Hz) show that at low frequencies (<1 Hz) the uncoated Fe_3O_4 exhibits a high impedance in the 1000 Ω range, whereas Fe_3O_4 @Pect displays a slightly lower |Z|. As the frequency increases, |Z| for both electrodes decrease and stabilizes at ∼100 Ω. The phase-angle spectra further differentiate the interfaces, with Fe_3O_4 @Pect showing a larger peak phase angle and a shift of the maximum toward higher frequencies, indicative of a faster interfacial time constant and stronger capacitive contribution. In contrast, the uncoated electrode presents a lower phase-angle maximum centered at lower frequency, consistent with sluggish interfacial kinetics. These Bode features corroborate the Nyquist findings of a reduced charge-transfer resistance for Fe_3O_4@Pect (R_{ct} = 447.21 Ω) relative to uncoated Fe_3O_4 (R_{ct} = 106,417 Ω), confirming that the pectin coating enhances charge-transfer kinetics.[102] The equivalent circuit models shown in Figure 6b suggest that the Fe_3O_4@Pect electrode possesses a more heterogeneous interface, likely reflecting dual charge storage mechanisms. This is reflected by the need for a more complex model incorporating two parallel R–Q elements, which may correspond to electrochemical processes occurring at distinct surface domains or through multiple ion transport pathways introduced by the pectin coating. In contrast, the uncoated Fe_3O_4 is adequately represented by a simpler Randles-type circuit, indicative of a more uniform but kinetically restricted interfacial behavior. Similar improvements in electrochemical behavior have been reported for polymer-coated electrodes, such as chitosan–methionine systems, where the introduction of hydrophilic groups facilitated ion transport and improved electrolyte accessibility.[103] These results reinforce the role of the pectin coating in enhancing the electrochemical performance of Fe_3O_4 toward HER. This conclusion is further supported by the chronoamperometric results (Figure S1), where the Fe_3O_4@Pect electrode rapidly reached and maintained a steady current, in contrast to the continuous current decline observed for the uncoated Fe_3O_4, demonstrating the coating's ability to protect the surface and sustain electrochemical activity.

4. Electrochemical Water Splitting

The electrocatalytic activity of uncoated Fe_3O_4 and Fe_3O_4@Pect nanoparticles toward the hydrogen evolution reaction was evaluated using linear sweep voltammetry in both near-acidic (0.1 M K_2SO_4, pH 6.37) and alkaline (0.1 M KOH, pH 12.83) media. The LSV curves and corresponding Tafel slopes for both materials are presented in Figure 7. To assess stability and reproducibility, approximately 15 LSV cycles were conducted for each sample under both near-acidic and basic conditions.

The onset potential is a critical parameter for evaluating and comparing the efficiency of electrocatalysts in water splitting applications, as it refers to the minimum potential (voltage) that must be applied to an electrode to initiate a significant electrochemical reaction.[104] Under near-acidic conditions (0.1 M K_2SO_4, pH 6.37), uncoated Fe_3O_4 exhibited an onset potential of −754 mV, while Fe_3O_4@Pect showed a slightly higher onset potential of −824 mV. The lower onset potential of uncoated Fe_3O_4 indicates that it requires less energy to initiate the hydrogen evolution reaction. Furthermore, uncoated Fe_3O_4 demonstrated a higher current density over the examined potential range, suggesting better catalytic activity under near-acidic conditions.

Under alkaline conditions (0.1 M KOH, pH 12.83), the onset potential for uncoated Fe_3O_4 was determined to be −484 mV, whereas Fe_3O_4@Pect exhibited a lower onset potential of −374 mV, indicating improved catalytic initiation in basic media. Interestingly, Fe_3O_4@Pect showed a higher current density during the initial stages of electrolysis; however, beyond −750 mV, uncoated Fe_3O_4 slightly surpassed Fe_3O_4@Pect in current density. This contrast in performance between near-acidic and basic media can be attributed to the pH-dependent behavior of pectin. Previous studies have shown that at low pH, high-methoxyl (HM) pectin tends to form gels, which can block some of the active sites on the Fe_3O_4 surface and reduce the frequency of effective collisions between the catalyst's active sites and the electrolyte. This results in decreased catalytic activity of the Fe_3O_4@Pect composite under acidic conditions.[105,106] In contrast, under alkaline conditions, pectin undergoes de-esterification, converting methyl ester groups into carboxylate ($-COO^-$) groups. These functional groups promote electron transfer processes, thereby enhancing the electrocatalytic performance of Fe_3O_4@Pect at high pH.[107,108] These results are consistent with previous reports on optimized nickel–cobalt and nickel–iron oxide catalysts for the hydrogen evolution reaction in alkaline media, where an onset potential of approximately −400 mV was achieved for Fe_3O_4-based catalysts.[109] Similarly, studies on iron oxide in electrochemical water splitting have reported an overpotential of 500 mV at a current density of 10 mA/cm^2, highlighting the inherently poor HER performance of bare iron oxide. However, the incorporation of a supporting material has been shown to significantly reduce the overpotential to as low as −260 mV which is a trend that aligns with the enhanced catalytic performance observed for the Fe_3O_4@Pect composite in this study.[110]

To evaluate the stability of the synthesized catalysts, multiple LSV cycles were performed under both acidic and alkaline conditions (Figure S2). A gradual decline in current density was observed with increasing cycle number, indicating some loss of catalytic activity over time. Under near-acidic conditions, the current density at −1.15 V decreased by approximately 4.00 mA/cm^2 for uncoated Fe_3O_4 and 1.92 mA/cm^2 for Fe_3O_4@Pect, suggesting comparatively better stability of the pectin-coated catalyst in near-acidic media. Since cathodic current density is directly proportional to the amount of hydrogen evolved, the

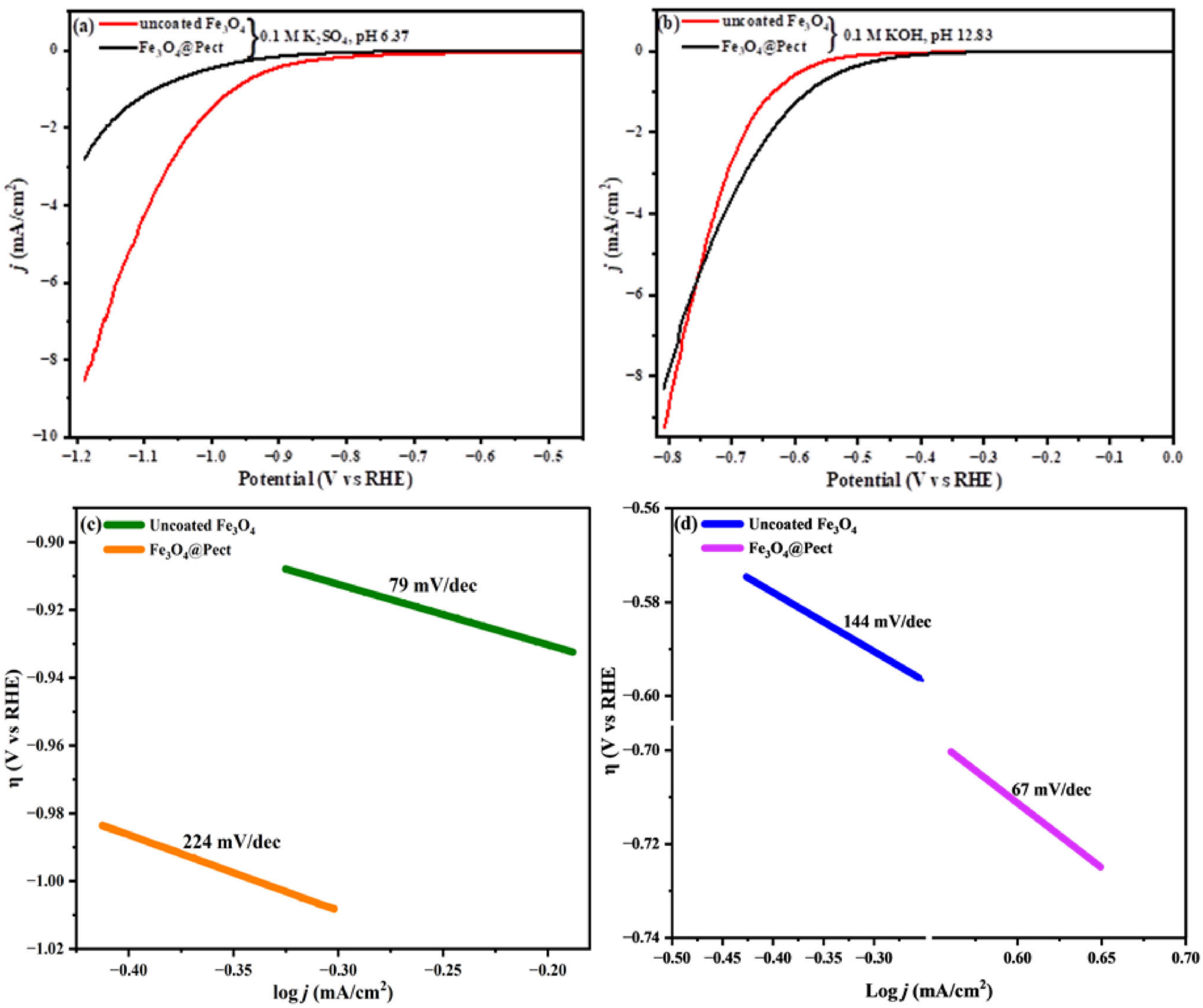

Figure 7. LSV traces of uncoated Fe_3O_4 (red), Fe_3O_4@Pect (black) in a) 0.1 M K_2SO_4 and b) 0.1 M KOH. c) Tafel slopes for uncoated Fe_3O_4 (green) and Fe_3O_4@Pect (orange) in 0.1 M K_2SO_4. d) Tafel slopes for uncoated Fe_3O_4 (blue) and Fe_3O_4@Pect (magenta) in 0.1 M KOH.

observed decline also reflects a reduction in hydrogen generation efficiency with continued cycling.[111] This trend was further supported by the current density differences observed under alkaline conditions, with declines of approximately 6.07 mA/cm^2 for uncoated Fe_3O_4 and 3.76 mA/cm^2 for Fe_3O_4@Pect. Although the relative decrease in current density was smaller at high pH compared to near-acidic conditions, the overall current densities remained significantly higher, as shown in Figure S2. The enhanced performance in alkaline media can be attributed to more efficient water dissociation, which improves catalytic activity. Additionally, the alkaline environment helps preserve the structural integrity of pectin, thereby contributing to the sustained catalytic performance of the metal nanoparticles.[37,112] This is consistent with the understanding that electrolyte pH alters catalyst–electrolyte interactions and proton availability, influencing parameters such as hydrogen binding energy, water adsorption, and overall reaction kinetics.[113]

These observations were further supported by Tafel analysis, which provides insight into the electron-transfer kinetics of the hydrogen evolution reaction. Tafel plots derived from the LSV polarization curves (Figure 7c,d) were used to calculate the Tafel slopes, with the values summarized in Table 2. A lower Tafel slope indicates more favorable electrocatalytic kinetics, whereas a higher value suggests slower reaction kinetics. In near-acidic medium, the Tafel slope for uncoated Fe_3O_4 was 79 mV/dec, while Fe_3O_4@Pect exhibited a higher slope of 224 mV/dec, corroborating the earlier observation of reduced performance under near-acidic conditions. Conversely, in alkaline medium, Fe_3O_4@Pect showed a significantly lower Tafel slope of 67 mV/dec compared to 114 mV/dec for uncoated Fe_3O_4, confirming its superior catalytic performance in basic environments. This enhanced performance under alkaline conditions suggests that HER on Fe_3O_4@Pect follows the Volmer–Heyrovsky mechanism, with the electrochemical desorption likely being the rate-limiting step. An additional contributing factor to the improved kinetics may be the presence of surface hydroxy groups introduced by the pectin coating, which facilitate water dissociation and promote more efficient hydrogen evolution at

Table 2. Electrocatalytic measurements of uncoated Fe_3O_4 and Fe_3O_4@Pect under near-acidic and alkaline conditions.

	0.1 M K_2SO_4 (near-acidic)		0.1 M KOH (alkaline)	
	Uncoated Fe_3O_4	Fe_3O_4@Pect	Uncoated Fe_3O_4	Fe_3O_4@Pect
Onset potential (mV)	−754	−824	−474	−374
Tafel slope (mV/dec)	79	224.4	144	67

the Fe_3O_4 active sites. Although BET analysis revealed a decrease in surface area and pore volume upon pectin functionalization, the rougher surface morphology and clustered structure observed for Fe_3O_4@Pect might have likely contributed to the additional catalytically active sites. Moreover, the introduction of hydrophilic functional groups such as –OH and $–COO^-$ enhances proton accessibility and local reaction kinetics. Under alkaline conditions, de-esterification of pectin generates additional $–COO^-$ groups, which may serve as electron-donating sites that facilitate charge transfer. These structural and chemical modifications collectively explain the lower onset potential and Tafel slope observed for Fe_3O_4@Pect in alkaline media, demonstrating that the nanoscale surface environment plays a pivotal role in tuning electrocatalytic activity.

5. Conclusion

In this study, high-purity pectin was successfully extracted from orange peels, exhibiting a degree of esterification of 66.3% (corresponding to 33.7% unesterified carboxyl groups), an ash content of 0.98%, and an AUA of 87.13%. The extracted pectin was employed as a stabilizing and functional support for Fe_3O_4 nanoparticles in electrocatalytic water splitting. Both uncoated Fe_3O_4 and Fe_3O_4@Pect composites were synthesized using established methods. Structural confirmation was achieved through FTIR and XRD analyses, while SEM-EDX provided insights into surface morphology and elemental composition, confirming the successful incorporation of pectin. BET analysis further supported successful surface modification, with reductions in surface area, pore volume, and pore diameter indicative of pectin coating. The electrocatalytic activity of these materials toward the hydrogen evolution reaction was assessed via linear sweep voltammetry in near-acidic and alkaline media. While both materials exhibited catalytic activity, Fe_3O_4@Pect demonstrated superior performance and durability, particularly under alkaline conditions. After 15 LSV cycles, Fe_3O_4@Pect showed a modest current density decrease of $\sim$1.93 mA/cm^2 under near-acidic conditions, compared to a greater decline of $\sim$4.00 mA/cm^2 for uncoated Fe_3O_4. Similarly, in alkaline media, Fe_3O_4@Pect retained its activity more effectively, with nearly half the current density loss observed for the uncoated counterpart. These findings highlight the stabilizing effect of the pectin layer, which improves catalyst durability and facilitates electron and proton transfer via its functional groups. Overall, this work demonstrates a sustainable and efficient strategy for enhancing the electrocatalytic performance of iron oxide nanoparticles using pectin, a biodegradable, nontoxic, and biocompatible biopolymer. The successful integration of pectin not only improves the structural and electrochemical stability of Fe_3O_4 nanoparticles but also opens new possibilities for green and cost-effective catalyst design in hydrogen energy applications.

Author Contributions

N.S. and **N.N.** contributed to the study conception and design. Material preparation and data collection were performed by **N.S**. Data analysis was performed by **N.S.**, **Z.M.**, **S.R.**, and **N.N**. The first draft of the manuscript was written by **N.S.**, and all authors commented on previous versions of the manuscript. All authors read and approved the final manuscript.

Acknowledgments

The authors thank the University of Pretoria for its support. N.S. thank the Department of Trade, Industry, and Competition of South Africa for the scholarship support. Z.M. thank the University of Pretoria for scholarship support.

Conflict of Interests

The authors declare no conflict of interest.

Data Availability Statement

The data that support the findings of this study are available from the corresponding author upon reasonable request.

Keywords: Electrochemical water splitting · Fe_3O_4 nanoparticles · Pectin

[1] X. Gao, Y. Chen, Y. Wang, L. Zhao, X. Zhao, J. Du, H. Wu, A. Chen, *Nano-Micro Lett.* **2024**, *16*, 237.
[2] Y. L. Pang, S. Lim, S. O. Lai, W. C Chong, in *Green Sustainable Process for Chemical and Environmental Engineering and Science* (Eds :Inamuddin, T. Altalhi, A. Alrooqi), Elsevier, Amsterdam **2023**, pp. 121–137, https://doi.org/10.1016/B978-0-323-95183-8.00003-2.
[3] S. Wang, A. Lu, C.-J Zhong, *Nano Convergence* **2021**, *8*, 4.
[4] K. Srinivas, Y. Lu, Y. Chen, W. Zhang, D. Yang, *ACS Sustainable Chem. Eng.* **2020**, *8*:3820–3831.
[5] E. B. Agyekum, C. Nutakor, A. M. Agwa, S. Kamel, *Membranes* **2022**, *12*, 173.
[6] Q. Hassan, I. D. J. Azzawi, A. Z. Sameen, H. M Salman, *Sustainability* **2023**, *15*, 11501.
[7] S. Chakraborty, S. K. Dash, R. M. Elavarasan, A. Kaur, D. Elangovan, S. T. Meraj, P. Kasinathan, Z. Said, *Front. Energy Res.* **2022**, *10*, 893475.

[8] S. F. Ahmed, M. Mofijur, S. Nuzhat, N. Rafa, A. Musharrat, S. S. Lam, A. Boretti, *Int. J. Hydrogen Energy* **2022**, *47*, 37227–37255.
[9] A. Zakariazadeh, R. Ahshan, R. Al Abri, M. Al-Abri, *Clean. Eng. Technol.* **2024**, *18*, 100722.
[10] R.-T. Gao, Y. Yang, X. Liu, X. Zhang, L. Wang, L. Wu, *Matter* **2024**, *7*, 2278–2293.
[11] R. Shahazi, A. I. Saddam, S. Majumdar, I. MdR, M. M. Rahman, A. MdM, A. Kumer, G. Paimard, *Charact. appl. nanomater.* **2024**, *7*, 5834.
[12] Z. Chen, S. Yun, L. Wu, J. Zhang, X. Shi, W. Wei, Y. Liu, R. Zheng, N. Han, B.-J Ni, *Nano-Micro Lett.* **2023**, *15*, 4.
[13] R.-T. Gao, Z. Gao, N. T. Nguyen, J. Chen, X. Liu, L. Wang, L. Wu, *Nat. Sustain.* **2025**, *8*, 672–681.
[14] D. Zhang, J. Z. Soo, H. H. Tan, C. Jagadish, K. Catchpole, S. K Karuturi, *Adv. Energy Sustain. Res.* **2021**, *2*, 2000071.
[15] K. Chen, G.-C. Kim, C. Kim, S. Yadav, I.-H Lee, *J. Colloid Interface Sci.* **2024**, *657*, 684–694.
[16] B. G. Pollet, S. S Kalanur, *Molecules* **2024**, *29*, 4990.
[17] P. I. Kyesmen, N. Nombona, M. Diale, *J. Alloys Compd.* **2021**, *863*, 158724.
[18] S. Delice, M. Isik, N. M Gasanly, *Chem. Phys. Lett.* **2024**, *840*, 141139.
[19] K. P. Thaba, M. M. Mphahlele-Makgwane, P. I. Kyesmen, M. Diale, P. G. L. Baker, P. R Makgwane, *Colloids Surf. A* **2022**, *633*, 127856.
[20] I. Safitri, Y. G. Wibowo, D. Rosarina, Sudibyo, *IOP Conf. Ser.: Mater. Sci. Eng.* **2021**, *1011*, 012020.
[21] A. K. Singh, D. Sarkar, *Nanoscale* **2018**, *10*, 13130–13139.
[22] J. Xue, N. Zhang, Q. Shen, Q. Li, X. Liu, H. Jia, R. Guan, *J. Alloys Compd.* **2022**, *918*, 165787.
[23] M. Mushtaq, P. U. Sathyakam, R. Vijayaraghavan, *Next Mater.* **2024**, *3*, 100159.
[24] M. Subash, M. Chandrasekar, S. Panimalar, C. Inmozhi, R. Uthrakumar, *Mater. Today Proc.* **2022**, *56*, 3413–3417.
[25] R.-T. Gao, J. Zhang, T. Nakajima, J. He, X. Liu, X. Zhang, L. Wang, L. Wu, *Nat. Commun.* **2023**, *14*, 2640.
[26] S. Meng, S. Sun, Y. Liu, Y. Lu, M. Chen, *J. Colloid Interface Sci.* **2022**, *624*, 433–442.
[27] R. Atchudan, T. N. J. Immanuel Edison, S. Perumal, R. Vinodh, N. Muthuchamy, Y. R Lee, *Fuel* **2020**, *277*, 118235.
[28] F. Samimi, M. Ghiyasiyan-Arani, *Int. J. Hydrogen Energy* **2024**, *91*, 423–433.
[29] Y. Niu, Q. Shi, T. Peng, X. Cao, Y. Lv, *Nanomaterials* **2025**, *15*, 681.
[30] I. N. Reddy, B. Akkinepally, J. Shim, C. Bai, *Crystals* **2024**, *14*, 734.
[31] J. Ge, R. R. Chen, X. Ren, J. Liu, S. J. H. Ong, Z. J Xu, *Adv. Mater.* **2021**, *33*, 2101091.
[32] X. Yan, G. Li, K. Shen, C. Wang, K. Wang, *Green Chem.* **2023**, *25*, 9394–9404.
[33] S. S. Sankar, G. Keerthana, K. Manjula, J. H. Sharad, S. Kundu, *Inorg. Chem.* **2021**, *60*, 4034–4046.
[34] A. Panda, H.-K. Cho, H. Kim, *Int. J. Mol. Sci.* **2023**, *24*, 9585.
[35] J. Xue, Y.-N. Jing, L.-L. Li, X.-L. Yin, Z.-F. Xu, J. Li, Y.-L. Wang, *Colloids Surf. A* **2024**, *685*, 133158.
[36] S. Ren, R. Gao, N. T. Nguyen, L. Wang, *Angew. Chem., Int. Ed.* **2024**, *63*, e202317414.
[37] A. K. Zharmagambetova, E. T. Talgatov, A. S. Auyezkhanova, F. U. Bukharbayeva, A. I Jumekeyeva, *Catalysts* **2023**, *13*, 1403.
[38] M. Grami, Z. Rafiee, *RSC Adv.* **2024**, *14*, 24175–24184.
[39] M. Yadav, K. Y. Rhee, S. J. Park, D. Hui, *Composites, Part B* **2014**, *66*, 89–96.
[40] K. S. Banu, P. Chakraborty, *Nano-Struct. Nano-Objects* **2024**, *39*, 101317.
[41] C. Das, S. Sen, T. Singh, T. Ghosh, S. S. Paul, T. W. Kim, S. Jeon, D. K. Maiti, J. Im, G. Biswas, *Nanomaterials* **2020**, *10*, 1615.
[42] T. S. A. Lemos, J. F. De Souza, A. R Fajardo, *Carbohydr. Polym.* **2021**, *265*, 118013.
[43] G. Bagherzade, H. Khashei siuki, P. Ghamari Kargar, *MedBioTech J.* **2021**, *05*, https://doi.org/10.22034/mbt.2021.135147.
[44] Y. Li, N. Li, W. Jiang, G. Ma, M. M Zangeneh, *Int. J. Biol. Macromol.* **2020**, *163*, 2162–2171.
[45] P. Kulal, V. Badalamoole, *Int. J. Biol. Macromol.* **2020**, *156*, 1408–1417.
[46] H. Twinomuhwezi, A. C. Godswill, D. Kahunde, *Am. J. Phys. Sci.* **2020**, *1*, 17–30.
[47] L. P. Ferreira, C. P. Reis, T. T. Robalo, M. E. Melo Jorge, P. Ferreira, J. Gonçalves, A. Hajalilou, M. M Cruz, *Nanomaterials* **2022**, *12*, 1870.
[48] F.-T. J. Ngenefeme, N. J. Eko, Y. D. Mbom, N. D. Tantoh, K. W. M Rui, *Open J. Compos. Mater.* **2013**, *3*, 30–37.
[49] A. B. Kute, D. Mohapatra, N. Kotwaliwale, S. K. Giri, B. P Sawant, *Agric. Res.* **2020**, *9*, 241–248.
[50] E. Abebe Alamineh, *Am. J. Appl. Chem.* **2018**, *6*, 51.
[51] D. R. Chowdhury, L. Spiccia, S. S. Amritphale, A. Paul, A. Singh, *J. Mater. Chem. A* **2016**, *4*, 3655–3660.
[52] O. Van Der Heijden, S. Park, R. E. Vos, J. J. J. Eggebeen, M. T. M Koper, *ACS Energy Lett.* **2024**, *9*, 1871–1879.
[53] A. MostJ, S. Sarkar, T. Sharmin, S. C Mondal, *Appl. Food Res.* **2024**, *4*, 100614.
[54] Y. Yu, L. Cui, X. Liu, Y. Wang, C. Song, U. Pak, K. H. Mayo, L. Sun, Y. Zhou, *Front. Nutr.* **2022**, *9*, 925050.
[55] N. S. Said, I. F. Olawuyi, W. Y Lee, *Gels* **2023**, *9*, 732.
[56] L. Yi, L. Cheng, Q. Yang, K. Shi, F. Han, W. Luo, D. S. Source, *Polymers* **2024**, *16*, 2883.
[57] A. V. Gomashe, M. A. Deolekar, *Int. J. Curr. Microbiol. Appl. Sci.* **2019**, *8*, 2278–2282.
[58] P. Karbuz, N. Tugrul, *J. Food Sci. Technol.* **2021**, *58*, 641–650.
[59] M. Güzel, Ö. Akpınar, *Food Bioprocess Technol.* **2019**, *115*, 126–133.
[60] C. V. Berenguer, C. Andrade, J. A. M. Pereira, R. Perestrelo, J. S Câmara, *Processes* **2022**, *11*, 20.
[61] X. Ma, J. Jing, J. Yu, J. Wang, H. Zhu, Z. Hu, *ACS Omega* **2021**, *6*, 1391–1399.
[62] K. Baraiya, V. K. Yadav, N. Choudhary, D. Ali, D. Raiyani, V. A. Chowdhary, S. Alooparampil, R. V. Pandya, D. K. Sahoo, A. Patel, J. G. Tank, *Gels* **2023**, *9*, 908.
[63] R. Sarkar, M. Roy, M. Alam, A. Sarkar, A. A. Alarfaj, S. A. Alharbi, M. J Ansari, *Discov. Food* **2025**, *5*, 19.
[64] T. H. Nguyen, H. X. N. Tran, T. T. Vu, T. T. L. Ho, T. T. V Nguyen, *Can Tho Univ. J. Sci.* **2022**, *14*, 99–108.
[65] Y. Chen, J.-G. Zhang, H.-J. Sun, Z.-J Wei, *Int. J. Biol. Macromol.* **2014**, *70*, 498–505.
[66] Y. Yu, P. Lu, Y. Yang, H. Ji, H. Zhou, S. Chen, Y. Qiu, H. Chen, *Sci. Rep.* **2024**, *14*, 9182.
[67] D. Ropartz, M.-C. Ralet, in *Pectin: Technological and Physiological Properties* (Ed: V. Kontogiorgos), Springer, Cham **2020**, pp. 17–36, http://link.springer.com/10.1007/978-3-030-53421-9_2.
[68] H. Mohamed, *MOJ Food Process. Technol.* **2016**, *2*, 31–38, https://doi.org/10.15406/mojfpt.2016.02.00029.
[69] L. Nalbandian, E. Patrikiadou, V. Zaspalis, A. Patrikidou, E. Hatzidaki, C. N. Papandreou, *Curr. Nanosci.* **2016**, *12*, 455–468.
[70] F. Ghasemy-Piranloo, F. Bavarsiha, S. Dadashian, *J. Sol-Gel Sci. Technol.* **2022**, *103*, 908–920.
[71] J. Safari, S. Gandomi-Ravandi, Z. Haghighi, *RSC Adv.* **2016**, *6*, 31514–31525.K.
[72] V. A. Niraimathee, V. Subha, R. S. E. Ravindran, S. Renganathan, *Int. J. Environ. Sustain. Dev.* **2016**, *15*, 227.
[73] M. Stoia, R. Istratie, C. Păcurariu, *J. Therm. Anal. Calorim.* **2016**, *125*, 1185–1198.
[74] Y. Wei, B. Han, X. Hu, Y. Lin, X. Wang, X. Deng, *Proc. Eng.* **2012**, *27*, 632–637.
[75] R. Y. Hong, S. Z. Zhang, G. Q. Di, H. Z. Li, Y. Zheng, J. Ding, D. G Wei, *Mater. Res. Bull.* **2008**, *43*, 2457–2468.
[76] W. S. Abou-Elseoud, E. A. Hassan, M. L Hassan, *Carbohydr. Polym. Technol. Appl.* **2021**, *2*, 100042.
[77] W. Zhang, L. Y. Zhang, X. J. Zhao, Z. Zhou, *J. Mol. Liq.* **2016**, *222*, 995–1002.
[78] R. K. Mishra, A. B. A. Majeed, A. K Banthia, *Int. J. Plast. Technol.* **2011**, *15*, 82–95.
[79] T. Tatarchuk, N. Danyliuk, I. Lapchuk, A. Shyichuk, V. Kotsyubynsky, *Mater. Today Proc.* **2022**, *62*, 5805–5811.
[80] J. Xu, C. Ju, J. Sheng, F. Wang, Q. Zhang, G. Sun, M. Sun, *Bull. Korean Chem. Soc.* **2013**, *34*, 2408–2412.
[81] M. Jabli, N. Sebeia, A. Bchetnia, *J. Polym. Environ.* **2023**, *31*, 4326–4337.
[82] M. S. A. Darwish, L. M. Al-Harbi, A. Bakry, *J. Therm. Anal. Calorim.* **2022**, *147*, 11921–11930.
[83] B. Prill, S. Yusan, *Part. Sci. Technol.* **2022**, *40*, 521–530.
[84] J. Kang, F. Li, Z. Xu, X. Chen, M. Sun, Y. Li, X. Yang, L. Guo, *JACS Au* **2023**, *3*, 2660–2676.
[85] H.-T. SA, *J. Alloys Compd.* **2023**, *968*, 171914.
[86] Y. Xie, F. Luo, Z. Yang, *Energy Rev.* **2024**, *3*, 100103.

[87] Z. Sun, S. Wang, C. Zhou, Z. Ma, F. Qian, *Biomass Convers. Biorefin.* **2024**, *14*, 20129–20141.
[88] K. M. Wani, R. V. S Uppaluri, *Appl. Food Res.* **2023**, *3*, 100345.
[89] J. Arora, K. G. Ramawat, J.-M Mérillon, in *Agricultural Waste: Environmental Impact, Useful Metabolites and Energy Production* (Eds: K. G. Ramawat, J.-M. Mérillon, J. Arora), Sustainable Development and Biodiversity, Springer Nature, Singapore **2023**, Vol.*31*, pp. 3–20, https://link.springer.com/10.1007/978-981-19-8774-8_1.
[90] S. Yurdakal, C. Garlisi, L. Özcan, M. Bellardita, G. Palmisano, in *Heterogeneous Photocatalysis*, Elsevier, Amsterdam **2019**, pp. 87–152, https://linkinghub.elsevier.com/retrieve/pii/B9780444640154000043.
[91] A. Muhammad, A. Shah, S. Bilal, *Materials* **2019**, *12*, 2854.
[92] X. Yang, G. Sui, D. Guo, D. Chu, J. Li, S. Na, M. Yu, D. Li, *Ionics* **2023**, *29*, 4115–4123.
[93] C. Kyomugasho, S. Gwala, S. Christiaens, Z. Jamsazzadeh Kermani, A. M. Van Loey, T. Grauwet, M. E Hendrickx, *Food Hydrocolloids* **2017**, *62*, 299–310.
[94] S. K. Verma, A. Thirumurugan, P. K. Panda, P. Patel, A. Nandi, E. Jha, K. Prabakaran, R. Udayabhaskar, R. V. Mangalaraja, Y. K. Mishra, A. Akbari-Fakhrabadi, M. J. Morel, M. Suar, R. Ahuja, *Mater. Today Bio* **2021**, *12*, 100131.
[95] H. Bülter, G. Denuault, S. Mátéfi-Tempfli, M. Mátéfi-Tempfli, C. Dosche, G. Wittstock, *Electrochim. Acta* **2016**, *222*, 1326–1334, https://doi.org/10.1016/j.electacta.2016.11.108.
[96] J. Aguedo, L. Lorencova, M. Barath, P. Farkas, J. Tkac, *Chemosensors* **2020**, *8*, 127.
[97] M. Fan, P. Li, B. Liu, Y. Gong, C. Luo, K. Yang, X. Liu, J. Fan, Y. Xue, *Nanomaterials* **2023**, *13*, 1909.
[98] S. Franger, P. Berthet, J. Berthon, *J. Solid State Electrochem.* **2004**, *8*, 218–223.
[99] T. N. Pham, S. T. Tanaji, J.-S. Choi, L. HU, I. T. Kim, Y.-C Lee, *RSC Adv.* **2019**, *9*, 10536–10545.
[100] X. Chen, C. Zhao, J. Ma, X. Sun, J. Li, H. Li, *SSRN* **2023**, 23, https://doi.org/10.2139/ssrn.44259920.
[101] J. S. Ko, M. B. Sassin, D. R. Rolison, J. W Long, *Electrochim. Acta* **2018**, *275*, 225–235, https://doi.org/10.1016/j.electacta.2018.04.149.
[102] L. ACh, M. I Prodromidis, *ACS Meas. Sci. Au* **2023**, *3*, 162–193, https://doi.org/10.1021/acsmeasuresciau.2c00070.
[103] S. F. Hamza, S. Shahen, A. M. Abdel–karim, A. A. El-Rashedy, A. M Hyba, *Sci. Rep.* **2025**, *15*, 15924.
[104] C. Batchelor-McAuley, *Curr. Opin. Electrochem.* **2023**, *37*, 101176, https://doi.org/10.1016/j.coelec.2022.101176.
[105] R. Chen, I. Ratcliffe, P. A. Williams, S. Luo, J. Chen, C. Liu, *Food Hydrocolloids* **2021**, *111*, 106219.
[106] M. Bakhtiarian, M. M Khodaei, *Sustain. Chem. Pharm.* **2023**, *36*, 101296.
[107] M. Nemiwal, T. C. Zhang, D. Kumar, *Carbohydr. Polym. Technol. Appl.* **2021**, *2*, 100164, https://doi.org/10.1016/j.carpta.2021.100164.
[108] O. A. Attallah, M. A. Al-Ghobashy, M. Nebsen, R. El-Kholy, M. Y Salem, *Environ. Sci. Pollut. Res.* **2018**, *25*, 18476–18483.
[109] A. Y. Faid, A. O. Barnett, F. Seland, S. Sunde, *J. Electrochem. Soc.* **2019**, *166*, F519–F533.
[110] M. A. Sayeed, J. Heron, J. Love, A. P O'Mullane, *Chem. Asian J.* **2020**, *15*, 4339–4346.
[111] M. Shaban, I. Kholidy, G. M. Ahmed, M. Negem, H. M. A. El-Salam, *RSC Adv.* **2019**, *9*, 22389–22400.
[112] H.-F. Zhong, H. Yin, D.-X. Zhang, L.-Y. Gan, P. Wang, *J. Phys. Chem. C* **2019**, *123*, 24220–24224.
[113] G. K. Gebremariam, A. Z. Jovanović, I. A Pašti, *Hydrogen.* **2023**, *4*, 776–806.

Manuscript received: April 10, 2025